Numerical simulations of pressure buildup and salt precipitation during carbon dioxide storage in saline aquifers

Qingliang Meng [a,*], Xi Jiang [b], Didi Li [c] and Qiyuan Xie [c]

[a] Beijing Institute of Space Mechanics & Electricity, Beijing 100094, China

[b] Engineering Department, Lancaster University, Lancaster LA1 4YR, United Kingdom

[c] Department of Safety Science Engineering & State Key Laboratory of Fire Science, University of Science and Technology of China, Hefei, Anhui 230026, China

*Corresponding author. Email: qlmeng@mail.ustc.edu.cn

Abstract

The storage of large amounts of carbon dioxide (CO_2) captured from fossil fuel fired power plants in deep saline aquifers can be an effective and promising measure for reducing the emissions of greenhouse gases. Massive CO_2 injection into saline aquifers may cause multi-scale phenomena such as pressure buildup in a large scale, CO_2 plume evolution in a medium scale and salt precipitation in a small scale. In this study, three-dimensional simulations are performed to investigate the propagation of pressure and the impact of salt precipitation on the process of large scale CO_2 injection into the saline aquifers. Apart from the different scales of the processes, the numerical results show clearly different behaviours of the pressure changes in saline aquifers with different boundaries. Different types of salt precipitation occur adjacent to the injection well, presenting distinct impacts on the fluid flow. Affected by salt precipitation, the porosity and permeability are reduced, leading to declined transportation and degraded injectivity with different boundary conditions. The interplay between pressure buildup and solid saturation is compared in saline aquifers with different boundary conditions.

Keywords: CO_2 storage, Pressure buildup, Salt precipitation, CO_2 plume, Numerical simulations

NOMENCLATURE

Symbols

d	diffusivity
$\mathbf{D}$	distance between meshes m and n
$\mathbf{g}$	gravitational acceleration
$\mathbf{k}$	permeability tensor
k_{rg}	the relative permeability of CO_2
$k_{r\mathrm{l}}$	the relative permeability of brine
$\mathbf{n}$	normal vector
P	pressure
$\mathbf{q}$	Darcy flux
S	saturation
t	time
T	temperature
V	volume
X	mass fraction
x, y, z	Cartesian coordinates

Greek symbols

Γ	area
μ	dynamic viscosity
ρ	density
Σ	summation
τ	tortuosity
ϕ	porosity
∇	gradient operator

Subscripts/superscripts

c	capillary, critical
i, j, m, n	index
s	solid
α, β	fluid phase

32

1. Introduction

Carbon dioxide storage in deep saline aquifers is potentially the most promising method for massively reducing the ever increasing amount of CO_2 in the global atmospheric environment because of combustion utilization of fossil fuels [1-3]. Massive CO_2 injection into the saline aquifers may cause multi-scale spatial phenomena, including pressure buildup occurred in a large scale [4-6], CO_2 plume in a medium size [4, 5] and the distribution of precipitation in a small dimension [7]. When large volumes of CO_2 are injected into saline aquifers, pressure buildup may be produced which can quickly propagate in a large space. At the temperature and pressure conditions for CO_2 storage, the injected CO_2 will tend to accumulate at the top of reservoir and spread out along the top caprock, as schematically shown in Fig. 1(a). Meanwhile, the injection of dry supercritical CO_2 will displace the resident brine immiscibly, combined with the evaporation of water, which may eventually cause the aqueous phase dry-out and salt precipitation near the injection well [7-14]. The spatial size of precipitation region is just a small fraction of the plume. These phenomena are of great importance to the safety of CO_2 storage. On the one hand, excessive pressurization may cause a series of problems, involving the caprock fracture, the pollution of shallow groundwater resources, and the seismicity [15-18]. On the other hand, salt precipitation may lead to salt blockage near the injection well, which would obstruct the transportation of CO_2 and the propagation of pressure to the far filed [7, 8]. Therefore, predicting the propagation of pressure and the impact of salt precipitation on injectivity is crucial to the security of CO_2 storage in saline aquifers.

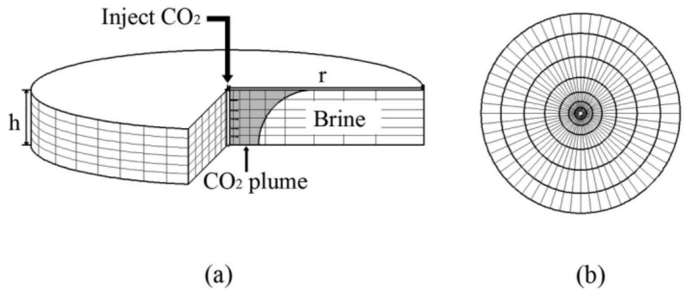

Fig. 1. Schematic representation of (a) CO_2 injection into an aquifer via a vertical well and (b) top view.

The pressure buildup during CO_2 injection into saline aquifers has been the focus of research by a number of theoretical analyses and numerical simulations. In terms of the theoretical analyses, several simple semi-analytical methods using Buckley-Leverett equation are used to study the distribution of pressure, which describe the one-dimensional immiscible flow in the absence of compression of rock pores and brine and capillary pressure [19-21]. Mathias et al. [4] improved the Buckley-Leverett method by incorporating the compressibility of rock and brine to study the pressure buildup during CO_2 injection into a closed saline aquifer. Zhou et al. [6] developed a quick assessment method of CO_2 storage capacity due to the formation and fluid compressibility, with assumptions that pressure buildup is spatially uniform and independent of formation permeability. Although these theoretical analyses may efficiently predict the pressure changes in some cases, detailed numerical simulations of carbon storage to calculate the pressure buildup including the spatial and temporal distributions are needed. For numerical studies, the important physical phenomena of pressure buildup are observed. Nonlinear behaviours of pressure change near wellbore during CO_2 injection into saline aquifers are observed [22]. Large-scale CO_2 injection could cause groundwater pressure perturbation and hydrological impact on groundwater resources [5, 17, 23, 24]. If the pressure buildup is above a threshold value, fracturing may occur. There is a stipulation by the U.S. Environment Protection Agency, stating that the maximum pressure must not exceed 90% of the fracture pressure in the injection zone [25]. Coupled reservoir geomechanical analyses are performed to check the fracture pressures by numerical simulations [26, 27]. Numerical simulations and optimization schemes are increasingly used to investigate this phenomenon, e.g. [28]. Optimization and parallel algorithms are also available to improve computation performance, e.g. [29-32]. The previous studies indicate that the pressure buildup in the injection zone is crucial to the security of CO_2 storage.

The process of salt precipitation has also been investigated by several theoretical analyses, experimental studies and numerical simulations. For theoretical analyses, Zeidouni et al. [10] developed a graphical method to determine the location of the front of solid salt. However, their results neglect the effects of the capillary pressure and the gravitational force. In addition their results are only applicable to a very simplified one-dimensional situation. For experimental studies, the reduction of permeability induced by drying of brine in porous media is studied for different rocks and salt contents [33]. A lab-on-a-chip approach is developed to study the pore-scale salt precipitation dynamics during CO_2 injection into saline aquifers [34]. Although experimental studies can provide first-hand results, detailed measurements are always difficult especially when information on flow quantities over a broad range of time and length scales is needed. In numerical studies, several researchers have shown that salt precipitates preferentially near the injection well as resident saline water is evaporated by injected CO_2 [7, 8, 14, 35-37]. For example, Hurter et al. [35] investigated the drying out and salting out phenomena using a commercial code. However, their results ignore the precipitation impact on permeability. Pruess and Müller [7] carried out one- and two-dimensional studies to predict salt precipitation and to understand the influencing factors for this process. Kim et al. [8] pointed out that there are two types of precipitation at different injection rates using two-dimensional simulations, which are characterized by different level of salt precipitation near the well. Their results suggest that great pressure buildup would occur near the lower portion of the injection well in some cases. These previous studies indicate that salt precipitation could cause reduction of aquifer porosity and permeability near the well and thus deterioration of injectivity.

Although some understandings on the impacts of pressure buildup and salt precipitation of CO_2 injection into the saline aquifers have been obtained, more studies are needed to understand the interplay between pressure buildup and salt precipitation. In previous numerical studies of salt precipitation in saline aquifers, the injection period is short and the injection rate was low, which does not meet the requirements of long-term and large-scale CO_2 storage. In the meantime, comparisons of the two phenomena in storage systems with different boundary conditions, namely the closed, open and semi-closed systems, are important but have not been investigated systematically.

In this study, the distributions of pressure buildup and salt precipitation, the specific processes and the impacts of solid precipitation on the long-term injection in the three storage systems are investigated by three-dimensional (3D) simulations. In the following, the governing equations together with the initial and boundary conditions used in the simulations are presented first, followed by numerical results and discussions of the results for the three systems investigated. Finally, some conclusions are drawn.

2. Modelling and mathematical formulation

2.1 Physical problem and computational domain

The physical problem is CO_2 injection and propagation, via a vertical well, into saline aquifers, as indicated in Fig. 1(a). The storage formation, located at a depth of approximate 1200 m below the ground surface, is 100 m thick with a radius of 40 km for the closed and semi-closed systems. The lateral extent of computation model for the open system is 100 km, which ensures that the lateral boundary could have a minimal effect on the simulation results.

2.2 Governing Equations

The governing equations for the fluid flows of multiphase and multicomponent fluid mixtures in porous media are used to describe CO_2 geological storage in saline aquifers [3], which are similar to those for oil, water, and gas flows through porous media. For isothermal problems, only the mass conservation equations for CO_2, water and salt are considered. The integral form of the mass equations for an individual *ith* species or component is given as [38]:

$$\frac{\partial}{\partial t}\int_{V_n}\phi\sum_{\alpha}\left(\rho_\alpha S_\alpha X_i^\alpha\right)dV_n+\int_{\Gamma_{\mathbf{n}}}\sum_{\alpha}\left(\rho_\alpha X_i^\alpha\mathbf{q}_\alpha\right)\cdot\mathbf{n}\,d\Gamma_{\mathbf{n}}-\int_{\Gamma_{\mathbf{n}}}\sum_{\alpha}\left(\phi S_\alpha\tau_\alpha d_i^\alpha\rho_\alpha\nabla X_i^\alpha\right)\cdot\mathbf{n}\,d\Gamma_{\mathbf{n}}=\int_{V_n}Q_i\,dV_n \qquad (1)$$

where $\mathbf{n}$ is the normal vector on the surface element $d\Gamma_n$ (assumed pointing inward into the mesh n). Eq. (1) is constructed by the balance of four terms representing all the possible mechanisms for mass transfer, which are the time rate of change of mass at a fixed point (or the local derivative or storage term), convective and diffusive transports, and source/sink term of mass respectively. $\mathbf{q}_\alpha$ can be defined by Darcy's law [39]:

$$\mathbf{q}_\alpha=-\frac{\boldsymbol{k}\,k_{r\alpha}}{\mu_\alpha}\left(\nabla P_\alpha+\rho_\alpha\mathbf{g}\nabla z\right) \qquad (2)$$

Eq. (2) is a multi-phase extension of Darcy's equation. Darcy's law is an approximate form of the fluid momentum balance in creeping flow through porous media. The law is only valid for steady, slow viscous flow, which can be derived from the Navier–Stokes momentum equations.

Eqs. (1)–(2) constitute the fundamental governing equations for the numerical simulations studied here. They are a coupled nonlinear system involving the geo-mechanical effects such as permeability and porosity of the solid rock matrix, multi-phase fluid properties like density and viscosity, which all affect the flow and transport behaviours. In order to close this mathematical problem, constitutive relationships and supplementary constraints for saturations, component compositions and pressures are needed [3].

The relative permeability $k_{r\alpha}$ is the ratio of the α phase permeability to the permeability of the porous medium. Under all-gas condition, the relative permeability of CO_2 is equal to 1.0. In order to close Eqs. (1)–(2), relationships for the relative permeability and capillary pressure are needed. In general, the two-phase characteristic curves are a function of the pore structure, phase saturation, surface tension, contact angle, and hysteresis [38].

The relative permeabilities of brine and CO_2 are calculated as follows:

$$k_{rl} = \sqrt{S^*}\left\{1 - \left(1 - \left[S^*\right]^{1/\lambda}\right)^{\lambda}\right\}^2 \tag{3}$$

$$k_{rg} = \left(1 - \hat{S}\right)^2 \left(1 - \hat{S}^2\right) \tag{4}$$

$$S^* = \left(S_l - S_{lr}\right) \big/ \left(1 - S_{lr}\right) \tag{5}$$

$$\hat{S} = \left(S_l - S_{lr}\right) \big/ \left(1 - S_{lr} - S_{gr}\right) \tag{6}$$

where k_{rl} and k_{rg} are the liquid and gas relative permeabilities, respectively. S_l is the liquid saturation, while S_{lr} and S_{gr} are the irreducible liquid and gas saturations, respectively. Eq. (3) for liquid is developed by van Genuchten [40]; eq. (4) for gas is due to Corey [41].

The formation for capillary pressure is given by van Genuchten [40]:

$$P_{c,\alpha\beta} = -P_0\left(\left[S^*\right]^{-1/\lambda} - 1\right)^{1-\lambda} \tag{7}$$

where P_0 is the strength coefficient, and λ is a parameter depending on pore geometry.

The difference of pressures between the two phases satisfies the following relation [39]:

$$P_\beta = P_\alpha + P_{c,\alpha\beta} \tag{8}$$

Eq. (8) shows that the fluid pressure in phase β is the sum of the gas phase pressure P_α and the capillary pressure $P_{c,\alpha\beta}$.

The evaporation model for H_2O partitioning into CO_2-rich phase is given by Spycher and Pruess model [42], which gives the mutual solubilities of CO_2 and H_2O in a non-iterative manner.

The salt precipitation due to the evaporation of injected CO_2 affects the fluid flows of gas and aqueous phases by changing the porosity and permeability of the formations. The solid salt occupies a fraction of the volume of the pores, which will lead to the decrease of space available for gas and aqueous phases. In this study, the solid salt is assumed to be immobile. Similar to the saturations of gas and aqueous phases, solid saturation is defined to describe the fraction of pore space occupied by salt precipitation.

In modelling the interplay between the two-phase flow and salt precipitation, it is important to specify the relationship between porosity and permeability. The underground formations contain different sizes of pores. Some precipitation can occur in the large pores, in which the permeability may not change much; others are found in the small pores, in which the permeability may decrease dramatically. The porosity-permeability relationship has been discussed by many investigators [14, 43, 44], whose results differ considerably from each other due to the complexity of the problem.

A tubes-in-series model is used to describe the permeability change due to the solid precipitation [44]. The model is composed of a series of parallel tubes with larger and smaller radii. The axes of the tubes are parallel to the fluid flows. The flow channels contain a great number of pore throats, hence even small changes in porosity may lead to dramatic permeability change due to the blockage of the pore throats. This permeability may be reduced to zero at a finite porosity, which can be defined as the “critical porosity”. In this study, the permeability decreases to zero when the porosity is reduced to 80% of its original value, i.e., when the solid saturation reaches 0.20.

2.3 Boundary and initial conditions

In terms of physical boundaries, the storage systems can be theoretically divided into three categories: (i) a closed system in which all the boundaries are impervious; (ii) an open system whose lateral boundaries are open so that the native brine can flow out; and (iii) a semi-closed system in which the lateral boundaries are impervious, while the storage formation is vertically bounded by sealing units with low permeability [6, 15]. For a closed system, the storage depends on the compressibility of the formation fluids and rock material as well as the dissolution rate of CO_2, which can provide expanded volumes available for storing the injected CO_2 [4, 16]. For an open system, the injected CO_2 displaces the brine laterally and is stored in the space that filled with aqueous phase [4-6]. For a semi-closed system, some fraction of the brine in the storage formation can migrate into the sealing units, which will increase the storage capacity for the injected CO_2 [6, 17, 18].

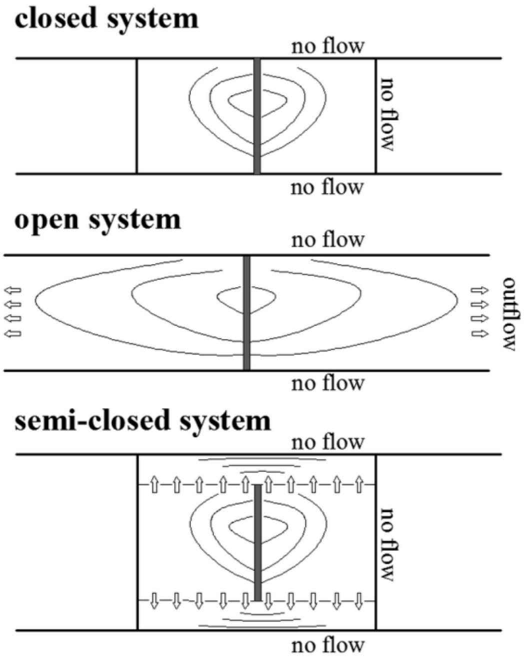

Fig. 2. Schematic representation of boundary conditions for the three storage systems: (a) open system, (b) closed system, and (c) semi-closed system.

All the boundaries for the closed and semi-closed systems are assumed to be impermeable to both supercritical CO_2 and brine except the wellbore boundary. For the open system, the volumes of grid blocks at the lateral boundary are assigned with an extremely large numerical value of 10^{50} m^3, thereby imposing a constant pressure condition at the far field. The top and bottom boundaries are also impervious. For the semi-closed system, two sealing formations with 60 m thick each are located at the top and the bottom of the storage system. The boundary conditions for the three storage systems are shown in Fig. 2.

Tab. 1. Hydrogeological properties of the storage formation.

Initial conditions	
Temperature	T = 45°C
Salinity	$X_s = 0.15$
Pressure	$P_{ini} \approx$ 120-131 bars
Dissolved CO_2 concentration	$X_1 = 0.$
Formation properties	
Horizontal permeability	$k_h = 10^{-12}$ m^2
Vertical permeability	$k_v = 10^{-12}$ m^2
Porosity	$\phi = 0.12$
Pore compressibility	$D = 4.5\times10^{-10}$ Pa^{-1}

Tab. 1 lists the assigned values of parameters used in this study, which are the typical conditions suitable for CO_2 storage. The formations are initially fully brine-saturated with the hydrostatic pressure distributing over the depths of the formations. The injection rate and injection period in the three systems are the same, which are 100 kg/s and 30 years, respectively. In order to examine the effect of the injection rate, a rate of 50 kg/s with injection period of 60 years is also considered for the closed system. Temperature is fixed at 45 °C throughout the simulations, representing an isothermal condition for the simulations considered here.

2.4 Numerical methods

The mass equations are discretized temporally using an implicit finite difference scheme and in space using an integral finite difference method as follows:

$$\begin{aligned}
&\left[\phi_n^{t+\Delta t}\sum_{\alpha}\left(\rho_{n,\alpha}^{t+\Delta t}S_{n,\alpha}^{t+\Delta t}X_{n,i}^{\alpha,t+\Delta t}\right)-\phi_n^{t}\sum_{\alpha}\left(\rho_{n,\alpha}^{t}S_{n,\alpha}^{t}X_{n,i}^{\alpha,t}\right)\right]\cdot\frac{V_n}{\Delta t}+\\
&\sum_{m}\left\{\left[\sum_{\alpha}\left(\rho_{\alpha,nm}^{t+\Delta t}X_{i,nm}^{\alpha,t+\Delta t}q_{\alpha,nm}^{t+\Delta t}\right)\right]\cdot\Gamma_{nm}\right\}-\\
&\sum_{m}\left\langle\left\{\sum_{\alpha}\left[\phi_{nm}^{t+\Delta t}S_{\alpha,nm}^{t+\Delta t}\tau_{\alpha,nm}^{t+\Delta t}d_{i,nm}^{t+\Delta t}\rho_{\alpha,nm}^{t+\Delta t}\left(X_{i,n}^{\alpha,t+\Delta t}-X_{i,m}^{\alpha,t+\Delta t}\right)\big/D_{nm}\right]\right\}\cdot\Gamma_{nm}\right\rangle\\
&=Q_{n,i}^{t}\cdot V_n
\end{aligned}\tag{9}$$

where $t + \Delta t$ represents the new time step, and flux terms are treated as fully implicit, given by the values at the new time step.

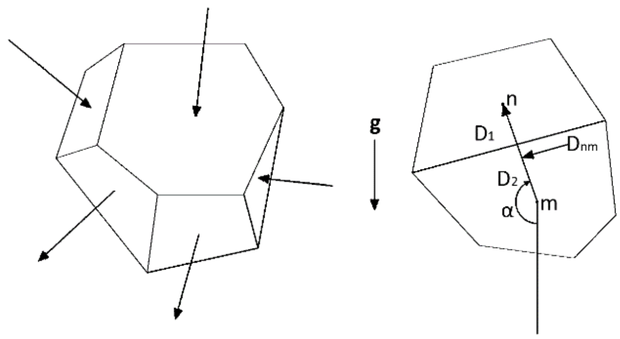

Fig. 3. Spatial discretization considered in this study.

The Darcy's law is discretized in the following way:

$$q_{nm}^{t+\Delta t}=-\left(\frac{k}{\mu}\right)_{nm}^{t+\Delta t}\left(\frac{P_n^{t+\Delta t}-P_m^{t+\Delta t}}{D_{nm}}-\rho_{nm}^{t+\Delta t}g\cos\alpha\right)\tag{10}$$

where α is the intersection angle between gravitational acceleration and the line segment from mesh m to n with rotation direction from g to the line segment clockwise as indicated in Fig. 3.

$$\cos\alpha=\frac{Z_2-Z_1}{D_1+D_2}\tag{11}$$

The variables in Eq. (9) - (10) on the interface are treated by distances harmonic averages method, given by,

$$f_{\alpha,nm}^{t+\Delta t} = \frac{D_1 f_{\alpha,m}^{t+\Delta t} + D_2 f_{\alpha,n}^{t+\Delta t}}{D_1 + D_2} \tag{12}$$

$$f = \left\{ \phi, S_\alpha, \tau_\alpha, d_i^\alpha, \rho_\alpha, h_\alpha, \lambda \right\} \tag{13}$$

A set of coupled nonlinear equations are obtained from Eq. (9)-(10). The compressed sparse row (CSR) format is adopted to store the sparse matrix linearized by the Newton-Raphson iteration [28, 45]. Nonzero elements of the matrix are stored in CSR format. Afterwards, the obtained system of linear equations is solved by parallel algorithm. In order to perform parallel simulations, domain decomposition method is used. The computational domain is decomposed into a number of subdomains. A global solution is formed through the local solutions on the subdomains. Solutions for subdomains can be sought simultaneously. In order to achieve better computational performance, each processor is assigned to the roughly the same number of meshes.

In order to track the process accurately and effectively, the temporal differencing is based on an automatic scheme, by changing the time steps according to the variations of solutions between adjacent time steps.

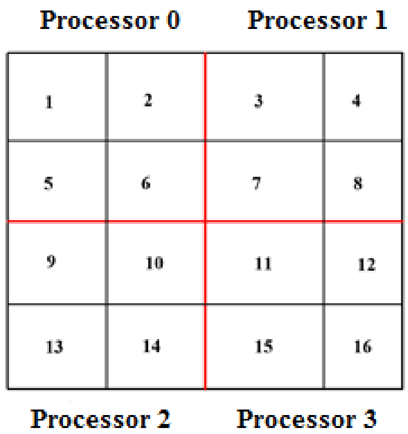

Fig. 4. A 16-meshes domain partitioning on 4 processors.

Fig. 4 shows a scheme for partitioning a sample domain with 16 meshes into four parts. Grids are assigned to four different processors and reordered to a local index ordering at each processor. The partitioned meshes are stored in each processor's update set. The update set is further divided into two subsets: internal and border. The solutions of elements in the internal subset only use the information on the current processor. The border subset includes grids that would require values from the other processors to be updated. An external set stores the meshes that are not in the current processor, which are needed to update the grids in the border set. Tab. 2 shows an example of the domain partitioning and local numbering.

Tab. 2. Example of domain partitioning and local numbering.

Processor		update		external
		internal	border	
Processor 0	Mesh	1	2，5，6	3，7，9，10
	Local Numbering	1	2，3，4	5，6，7，8
Processor 1	Mesh	4	3，7，8	2，6，11，12
	Local Numbering	1	2，3，4	5，6，7，8
Processor 2	Mesh	13	9，10，14	5，6，11，15
	Local Numbering	1	2，3，4	5，6，7，8
Processor 3	Mesh	16	11，12，15	7，8，10，14

Local Numbering	1	2，3，4	5，6，7，8

Communication between processors is an essential task of the parallel algorithm. Global communication is used to contribute grid blocks to all processors and check the convergence. In order to solve the linear equation system, communications between adjacent processors and linear solver routine are needed. When the meshes are in the border subset, exchange of data corresponding to the external set is performed.

2.5 Grid dependence tests

In order to obtain a better understanding on how the grid resolution affects numerical solutions, grid dependence is examined for the 3D closed system. Four different sets of grids in the range of 1.5–12 million are used to evaluate the dependence of the results on the grid number and determine the optimum number of grids, as shown in Fig. 5. The plots show the radial distributions of pressure buildup (compared with the initial pressure) and solid saturation at 10 days and 100 days along the top aquifer. It is evident that the optimal number of grids is 6 million by considering the computational accuracy and the efficiency.

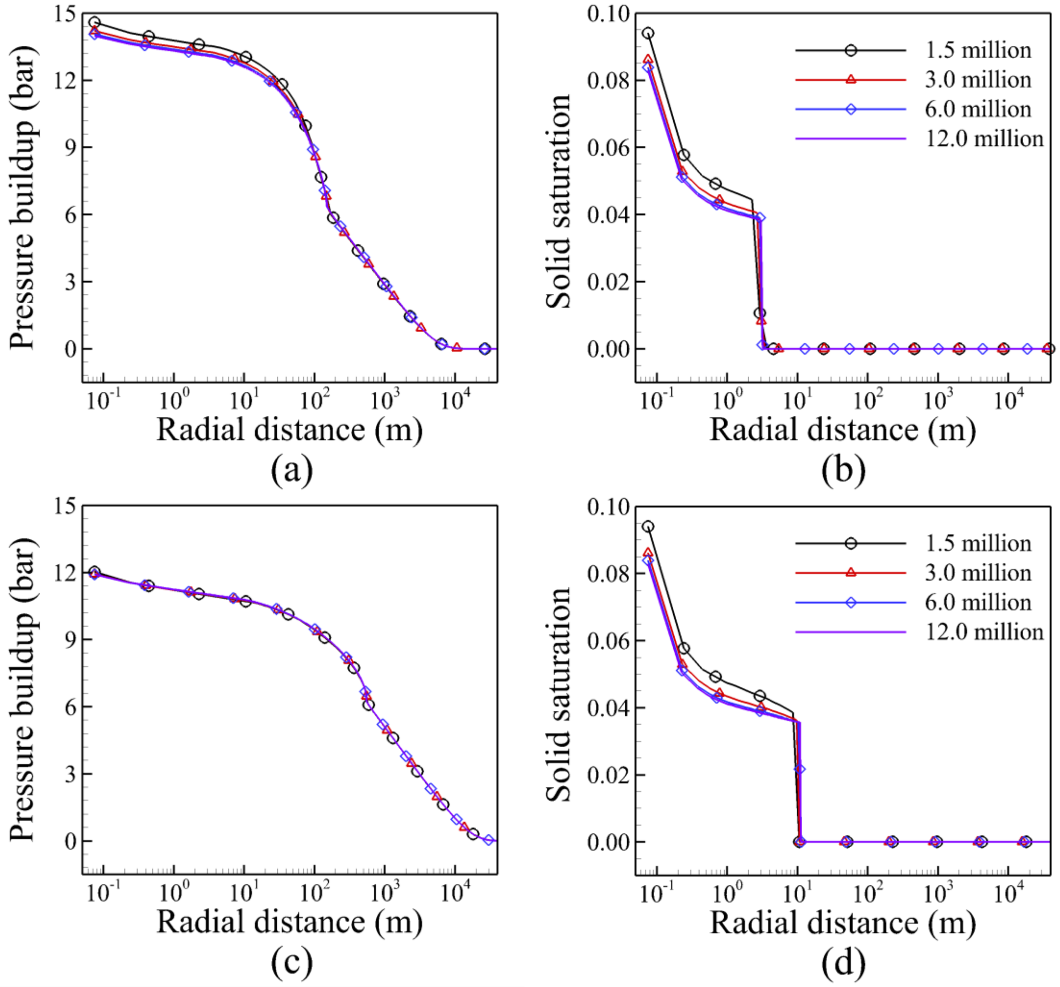

Fig. 5. The radial profiles of pressure buildup and solid saturation at the aquifer top for 10 days (top) and 100 days (bottom) for the grid dependence tests.

In this meshing system, the computation domain is discretized into 1000 grids in the radial direction, 60 grids in the axial direction and 100 grids in the vertical direction. The grid size increases logarithmically from the injection well, with the finest grid located close to the wellbore and the coarsest at the far side boundary in the radial direction. Every circle of the mesh in the axial direction is divided uniformly, and the targeted formation is also divided uniformly in the vertical direction. Similar meshing methods for the open and semi-closed systems are adopted, except that the target formation for the semi-closed system is divided into 220 grid blocks in the vertical direction.

3. Results and discussion

3.1 The results of the closed system

The snapshots shown in Fig. 6 correspond to the cross sections of pressure buildup and gas saturation at the end of the 30-year injection period. When large volumes of CO_2 are injected into this system, a significant pressure buildup is produced. The range of pressure perturbation covers the whole domain, with an elevated pressure of 31.5 bars near the injection well and of 26.0 bars at the lateral boundary shown in Fig. 6(a). The radius of CO_2 plume region is about 6 km and the plume is concentrated at the top portion of the aquifer, as shown in Fig. 6(c). It is clear that the scale of elevated pressure is much larger than the CO_2 plume size. The contour lines of pressure buildup in the CO_2 plume region shown in Fig. 6(b) are inclined, caused by the buoyancy and nonlinearity inherent in the two-phase flow system [3]. Meanwhile the contour lines away from the CO_2 plume region are mostly vertical, indicating a horizontal brine displacement.

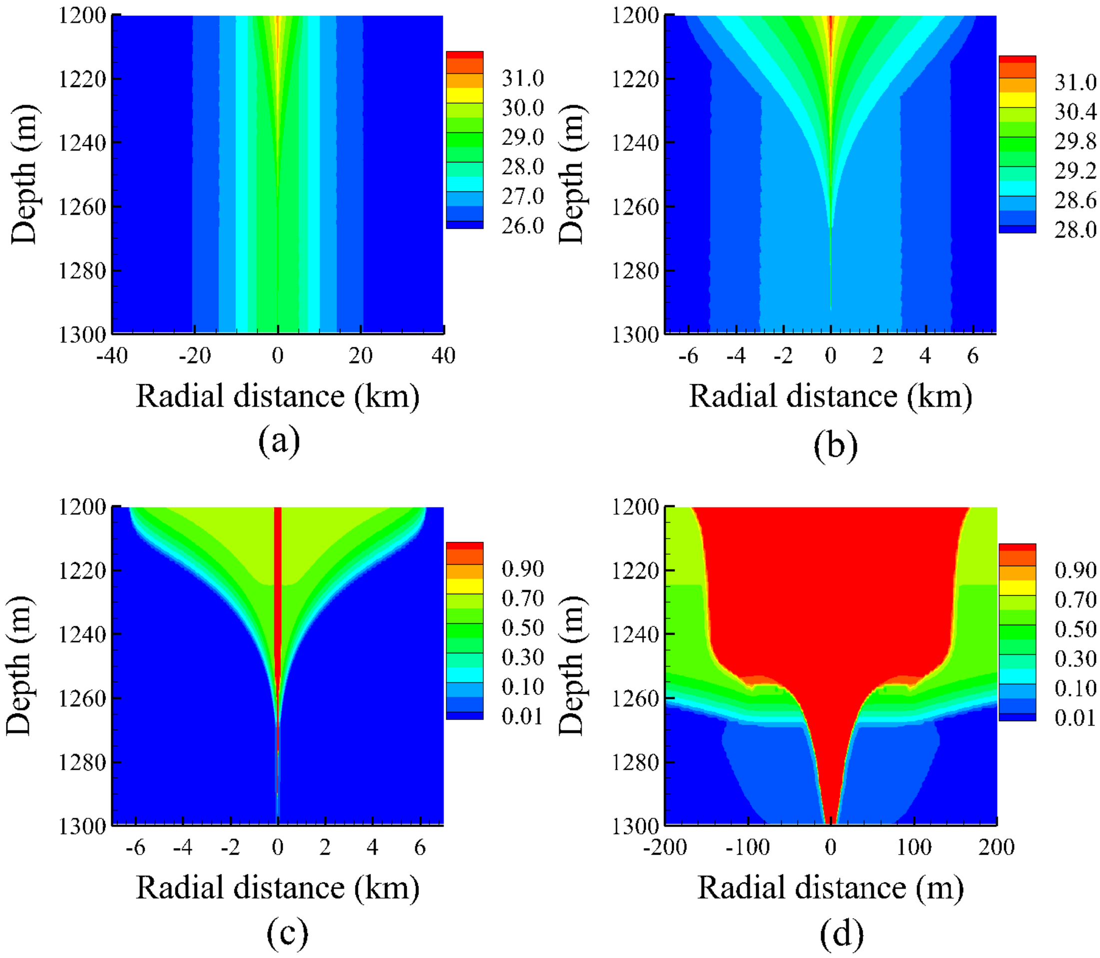

Fig. 6. Cross sections of pressure buildup (top: (b) is a zoom-in of (a)) and gas saturation (bottom: (d) is the zoom-in of (c)) for the closed system at 30 years of CO_2 injection; pressure unit: bar.

Due to the evaporation of dry gas, salt precipitation occurs near the well. In order to better capture the dynamic behaviours of precipitation, the horizontal grid size is set to be 0.15 m near the well, and increases logarithmically from the injection well. For the domain shown in Fig. 7, in which salt precipitation takes place, there are 257 grids along the horizontal direction. The precipitation distribution is controlled by the buoyancy driven CO_2 plume, which presents two kinds of precipitation, i.e., non-localized salt precipitation with smaller values and localized salt precipitation with larger values (shown in the closed-up view). Compared with the contour map of gas saturation near the well in Fig. 6(d), the non-localized precipitation occurs inside the zone of single gas phase and the localized precipitation is located at the lower portion of the dry-out front. The highest solid saturation in the localized salt precipitation region amounts to 0.20, which results in a zero permeability.

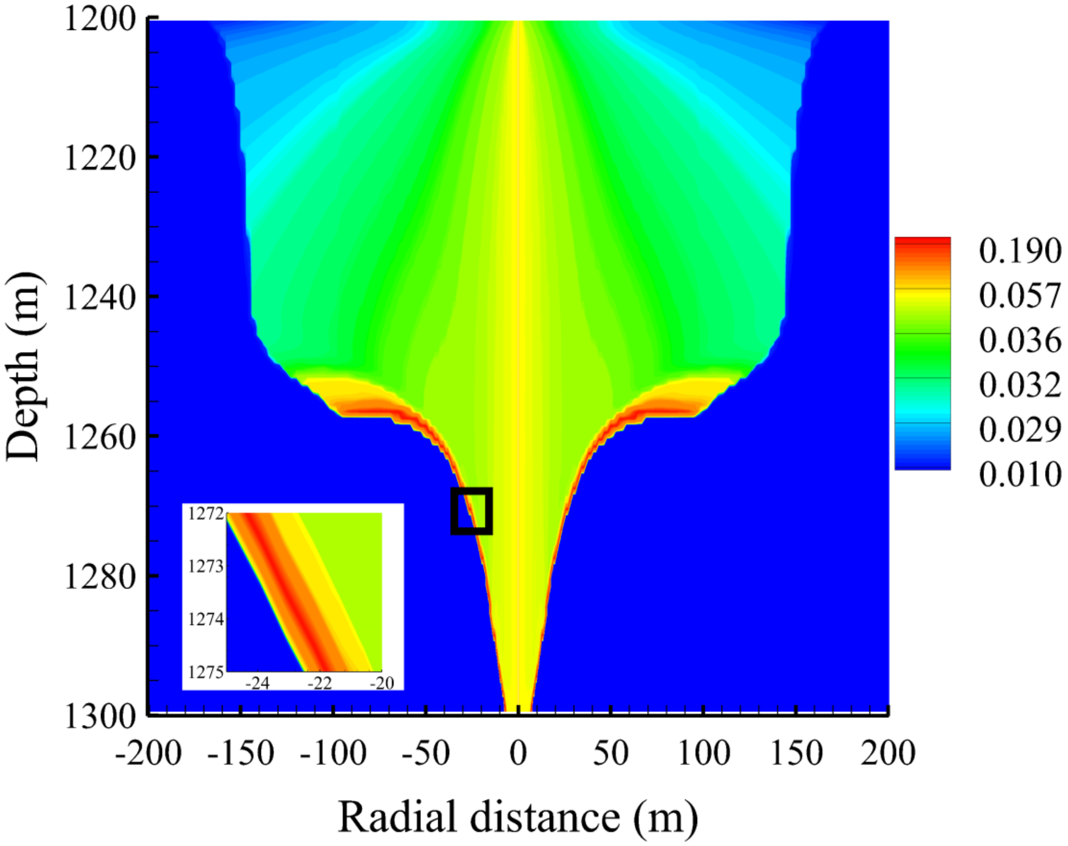

Fig. 7. Cross sections of solid saturation for the closed system at 30 years of CO_2 injection with a close-up view of non-localized precipitation.

The solid saturation iso-surfaces at different time instants are shown in Fig. 8, where the 3D results are shown for a three-quarter of the computational domain. The precipitation begins from the injection well and develops with time. Different zones of solid saturation present different behaviours with time, that is to say, the upper zone evolves continuously, while the lower zone tends to be stabilized.

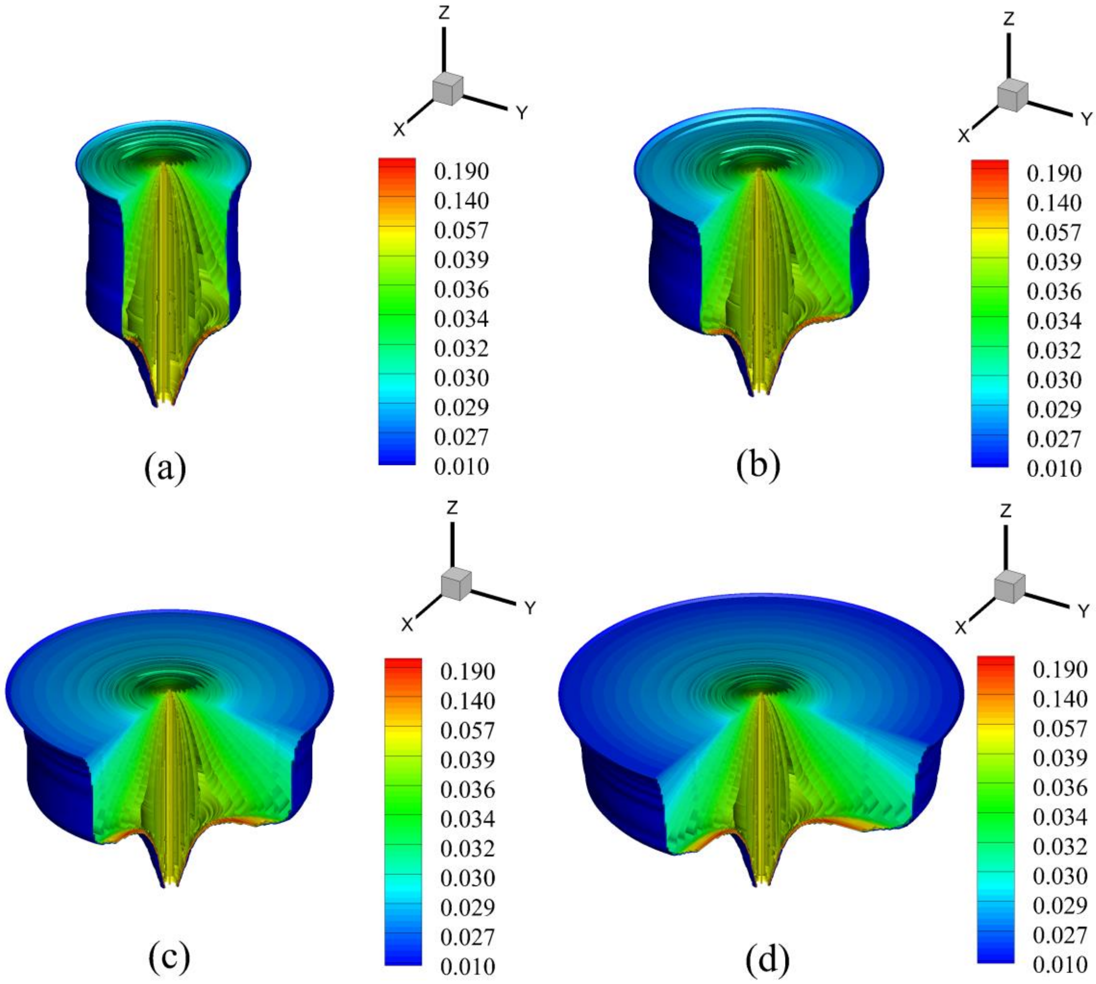

Fig. 8. Instantaneous iso-surfaces of solid saturation for the 3D closed system at different time instants.

Fig. 9 shows the temporal evolution of gas saturation and solid saturation, to illustrate the processes of the two types of precipitation. At the early stage, the injected CO_2 mainly displaces the resident brine, accompanied by interphase mass transfer of both CO_2 and brine between the aqueous phase and gas phase. When the brine becomes fully saturated due to the evaporation, the salt can quickly precipitate, corresponding to the quick increase of solid saturation. These trends for the two variables stop for the non-localized precipitation in Fig. 9(a). However, these trends still continue for the localized precipitation in Fig. 9(b). The capillary pressure overcomes the injection pressure, driving the brine towards the evaporation front. The backflow of aqueous phase can increase the solid saturation and decrease the gas saturation. Under the evaporation of gas phase, the precipitation front becomes thicker and more spread out, representing the increase of solid saturation. Once the solid saturation reaches 0.20, the composition of phases will not be changed.

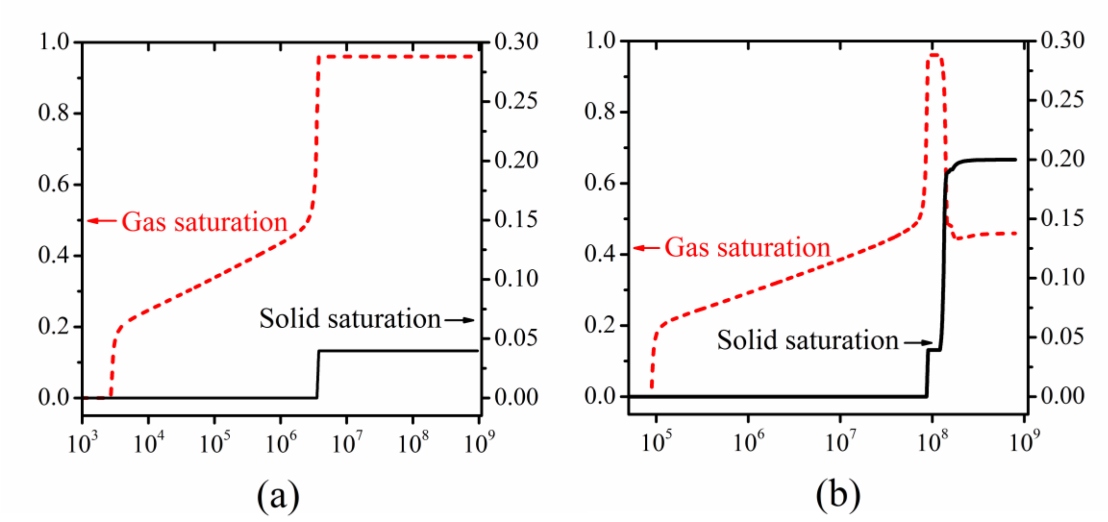

Fig. 9. The temporal evolution of gas saturation and solid saturation in (a) the non-localized precipitation region, (b) the localized precipitation region.

The pressure buildup along the bottom aquifer in Fig. 10(a) shows complicated behaviours. Simulation results predict an initial jump followed by a quick decline and then a gradual increase in near wellbore pressure over time. The pressure at these locations away from the injection well increases monotonously with time. Most notably, the curves demonstrate a pressure jump in the position of 8 m after an injection period of five years, and the values of pressure jump increase with the injection time, as marked by the green circles in Fig. 10(a). The differences of pressure are 0.38 bar for 5 years, 0.50 bar for 10 years, 0.70 bar for 20 years, and 0.89 bar for 30 years, which show an approximately linear behaviour.

The zone of solid precipitation in Fig. 10(b) spreads with the injection time. At the early stage (less than 100 days), the solid saturation zone spreads with time. As the brine is displaced gradually by the injected CO_2, the amount of precipitable salt declines with the increasing distance from the injection well, which in turn leads to the decrease of solid saturation. After 1 year injection, the backflow of brine occurs, resulting in a sharp gradient of solid saturation. Compared with the results in Fig. 10(a), the location of the gradient of solid saturation corresponds to the location of pressure jump. When the solid saturation amounts to 0.20, the pores are clogged completely and the horizontal flows of gas and aqueous phase are suppressed. During the subsequent stages, the profiles of gas and solid saturations remain unchanged.

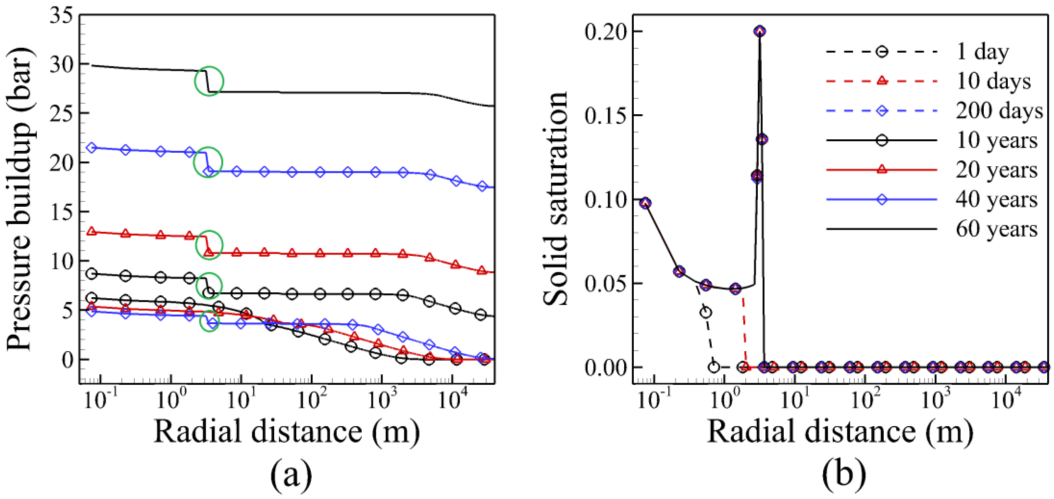

Fig. 10. Profiles along the bottom of the aquifer for the closed system at different injection time instants for (a) pressure buildup and (b) solid saturation.

The results of lower injection rate of 50 kg/s with the same total amount of CO_2 are given in Fig. 11-12. The values of hydrogeological parameters used in this model are given in Tab 1.

Fig. 11 shows the cross sections of gas and solid saturations with injection rate of 50 kg/s at the end of the injection period of 60 years. Compared with the larger injection rate case, there are obvious differences in the shapes of these distributions. The horizontal spread of the gas phase is reduced while the vertical movement is enhanced. Similar to the larger-rate case, the solid salt appears in the zone of single gas phase. Rather different precipitation behaviours are observed at the lower rate. The distribution radii of solid precipitation zone are smaller near the lower portions of the well, while the radii are larger near the upper portions of the well. The accumulation of solids in this case exacerbates gravity override effect, which means that more gas phase accumulates at the top aquifer. The distribution of gas phase increases the risk of leakage and reduces the security of CO_2 storage. The narrower zone at the bottom of the aquifer attenuates the pressure jump, which can be clearly seen in Fig. 12(a).

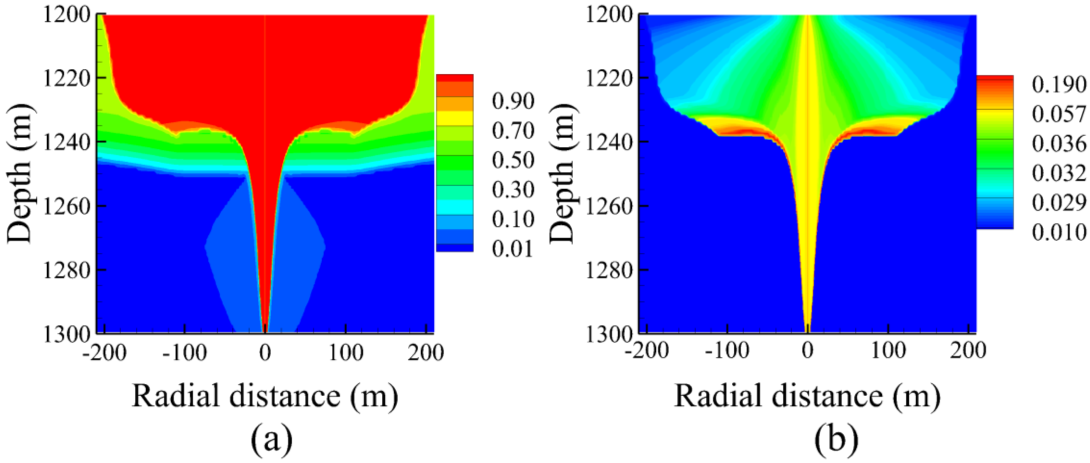

Fig. 11. Spatial distributions for the closed system at 60 years of CO_2 injection of (a) gas saturation and (b) solid saturation.

Fig. 12 shows the cross sections of pressure buildup and solid saturation at different time instants. Compared with the larger-rate case, the increment of pressure is slightly lower, while the values of pressure jump are higher at the bottom of the aquifer, as marked by the green circles in Fig. 12(a). The differences of pressure are 0.73 bar for 200 days, 1.50 bars for 10 years, 1.66 bars for 20 years, 1.94 bars for 40 years, and 2.15 bars for 60 years, respectively. The value of solid saturation at the injection well is 0.0975, which is 16 percent higher than that in Fig. 10(b). The distance between the impervious barrier and the wellbore is shorter, which is only 3.2 m. All of these factors could increase the possibility of fracture near the lower portion of injection well.

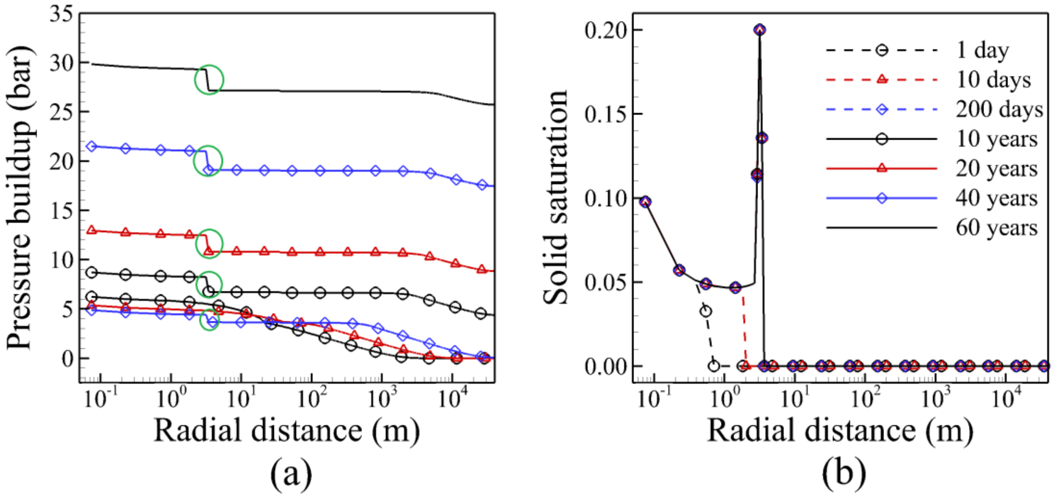

Fig. 12. Profiles along the bottom of the aquifer for the closed system with injection rate of 50 kg/s at different injection time instants for (a) pressure buildup, and (b) solid saturation.

3.2 The results of the open system

The snapshots shown in Fig. 13 correspond to the cross sections of pressure buildup, gas and solid saturations for the open system at the end of the 30-year injection period. Compared with the results in the closed system, a significant difference in the contour maps of pressure buildup is observed. The values of pressure buildup are lower, with maximum value of 9.5 bars at the top of the injection well. In marked contrast to the difference in the distribution of pressure buildup, minor differences in the CO_2 plumes and solid saturation distributions are observed. Comparison of the results in the closed and open systems indicates that the shapes of gas and solid phase distributions for the two storage systems are generally similar, with a larger distance in the lateral extent of the plume for the open system. The differences in the CO_2 plumes are caused by the differences in pressure buildup.

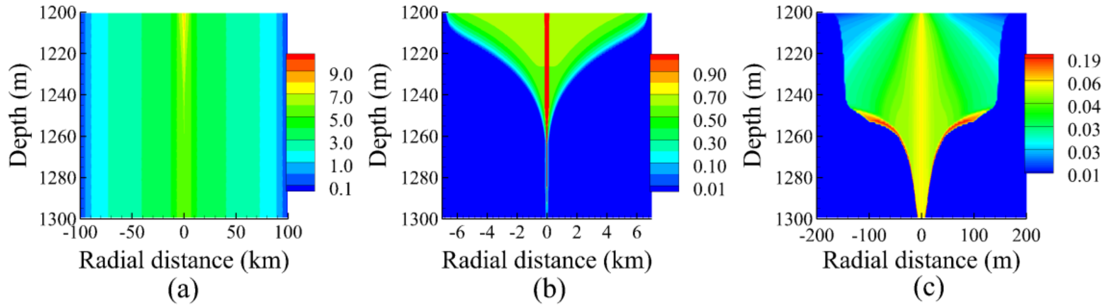

Fig. 13. Cross sections of (a) pressure buildup (unit: bar), (b) gas saturation and (c) solid saturation for the open system at 30 years of CO_2 injection.

Fig. 14 shows the radial profiles of pressure buildup and solid saturation at the same time instants as the closed system throughout the injection period. The profiles of pressure buildup show different behaviours compared with those in Fig. 10. Simulation results predict an initial jump followed by the continuous decline in the pressure near wellbore over time, while the pressures in the other region increase slightly. As the outflow rates of brine at the lateral boundaries are constant, the pressure changes in the whole domain are not obvious. Meanwhile, the pressure profiles along the bottom aquifer also present a jump near the well due to the localized precipitation. The radial profiles of solid saturation in the closed and open systems are generally similar, with minor differences in the radial distance of solid saturation along the bottom surface of the aquifer.

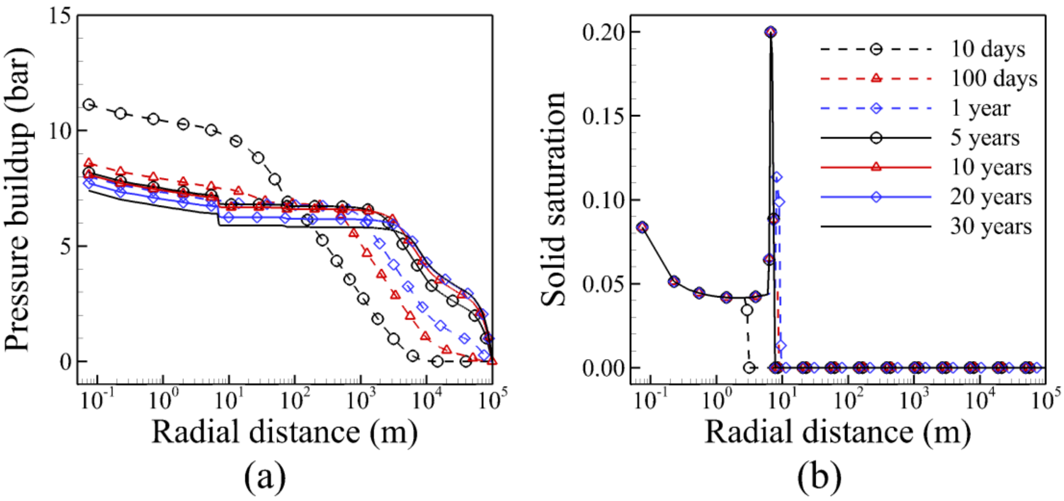

Fig. 14. Profiles along the bottom of the aquifer for the open system at different injection time instants for (a) pressure buildup (unit: bar), and (b) solid saturation.

3.3 The results of the semi-closed system

Fig. 15 shows the cross sections of pressure buildup with seal permeabilities of 10^{-17} m^2, 10^{-18} m^2 and 10^{-19} m^2 at the end of the 30-year injection period. In these cases, a small fraction of the brine in the storage formation is displaced into the overlying and underlying formations during the injection period, which can provide additional storage space for CO_2. Hence less pressure buildup occurs in the semi-closed system compared with the results in Fig. 6(a). The pressure buildup in the storage formations is very sensitive to the seal permeability. In the lowest seal permeability (10^{-19} m^2) case, the pressure buildup shows similar behaviours to those in the closed system. The propagation of elevated pressure is mainly in the storage formation. The values of pressure buildup in the storage formations are much higher than the values in the seal formations. In the medium seal permeability (10^{-18} m^2) case, the elevated pressure in the storage saline is lower than that in the lowest seal permeability case. More native brine in the storage formation is discharged into the seal formations. In the largest seal permeability (10^{-17} m^2) case, the propagation of elevated pressure is dominant in the vertical direction. With the increase of the fraction of brine leakage into the seal formation, more space is provided for the injected CO_2 in the storage formation. The zones of higher pressure buildup are all located in the two-phase regions for the three cases, which are the same as the distributions in the closed and open systems.

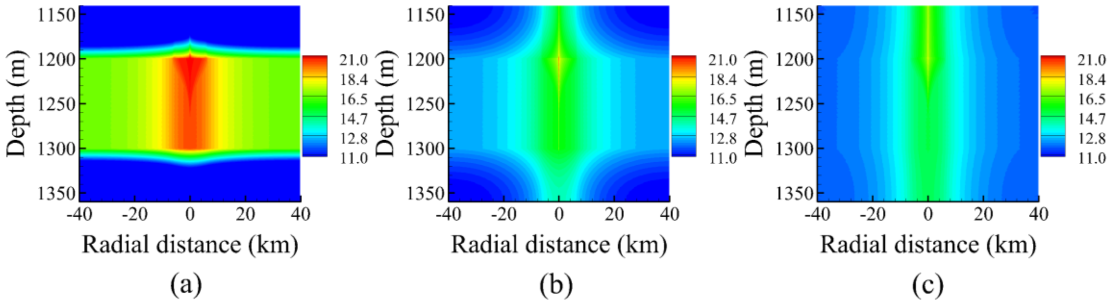

Fig. 15. Cross sections of pressure buildup (unit: bar) with seal permeabilities of (a) 10^{-19} m^2, (b) 10^{-18} m^2, and (c) 10^{-17} m^2 for the semi-closed system.

Fig. 16 shows the cross sections of solid saturation with three different seal permeabilities, where (a2-c2) are the zoom-in graphs of (a1-c1). In contrast to the distribution of pressure buildup, the solid saturation is less sensitive to the seal permeability. Comparison of Fig. 16 (a1-c1) indicates that the contour maps of solid precipitation in all the semi-closed cases are generally similar in shape, with several minor differences at the top of the storage formations. In addition to the two types of precipitation near the injection well (i.e., non-localized salt precipitation of smaller values, localized salt precipitation of larger values), the third type of solid precipitation occurs at the interfaces between the storage formation and the seal formations. At the interfaces, injected CO_2 in the storage saline hardly enters into the seal formations, which needs to overcome a considerable capillary entry pressure. Consequently, the flow of single gas phase at the interfaces can be suppressed and thus more salt can precipitate at these locations. With the increase of seal permeability, both the thickness of this kind of precipitation and the maximum value of salt precipitation in this zone increase. The higher precipitation zones at the interfaces contribute to reducing the leakage rate of gas phase from the storage saline into the seal formations.

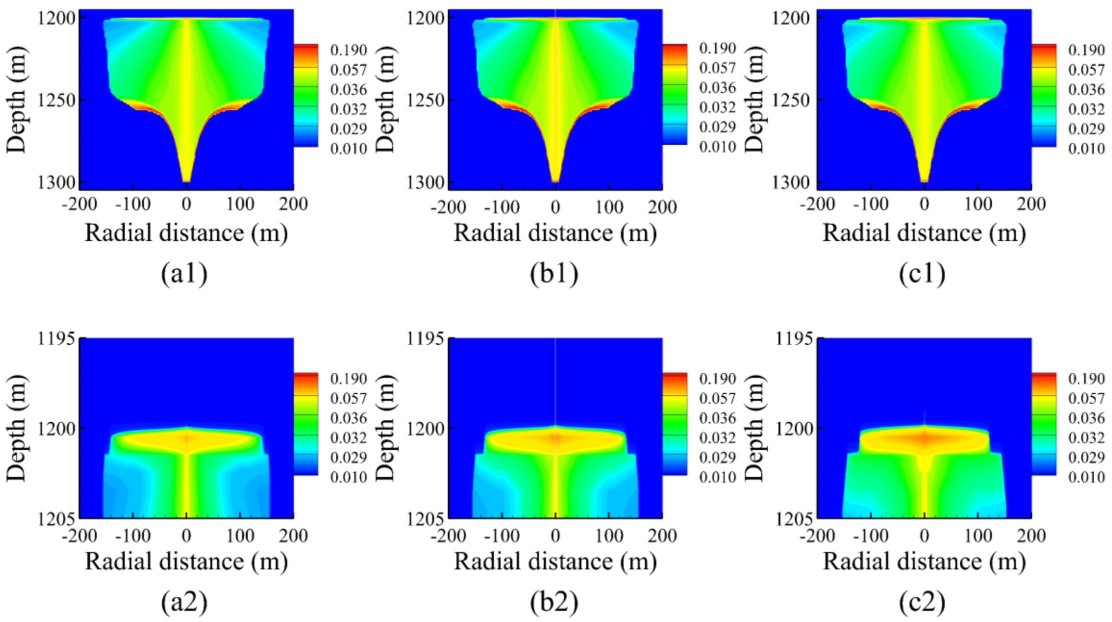

Fig. 16. Cross sections of solid saturation with seal permeability of (a1, a2) 10^{-19} m^2, (b1, b2) 10^{-18} m^2, and (c1, c2) 10^{-17} m^2 for the semi-closed system.

Fig. 17 shows the radial profiles of pressure buildup and solid saturation for the semi-closed system with seal permeability of 10^{-19} m^2 at different time instants throughout the injection period. The profiles of pressure buildup show similar behaviours to those of the closed system. Due to the leakage of brine into the seal formations, the values of pressure buildup at the top and bottom aquifer are lower. The pressure profiles along the bottom aquifer also show a jump near the wellbore. The values of salt saturation near the well increase during the whole injection period, which are different from those in the closed and open storage systems. Due to the lower seal permeability and the capillary pressure, the injected CO_2 hardly enters into the seal formations. The injected CO_2 will accumulate under the interface and evaporate the water in the brine at the interfaces continuously, which leads to the increase of solid saturation.

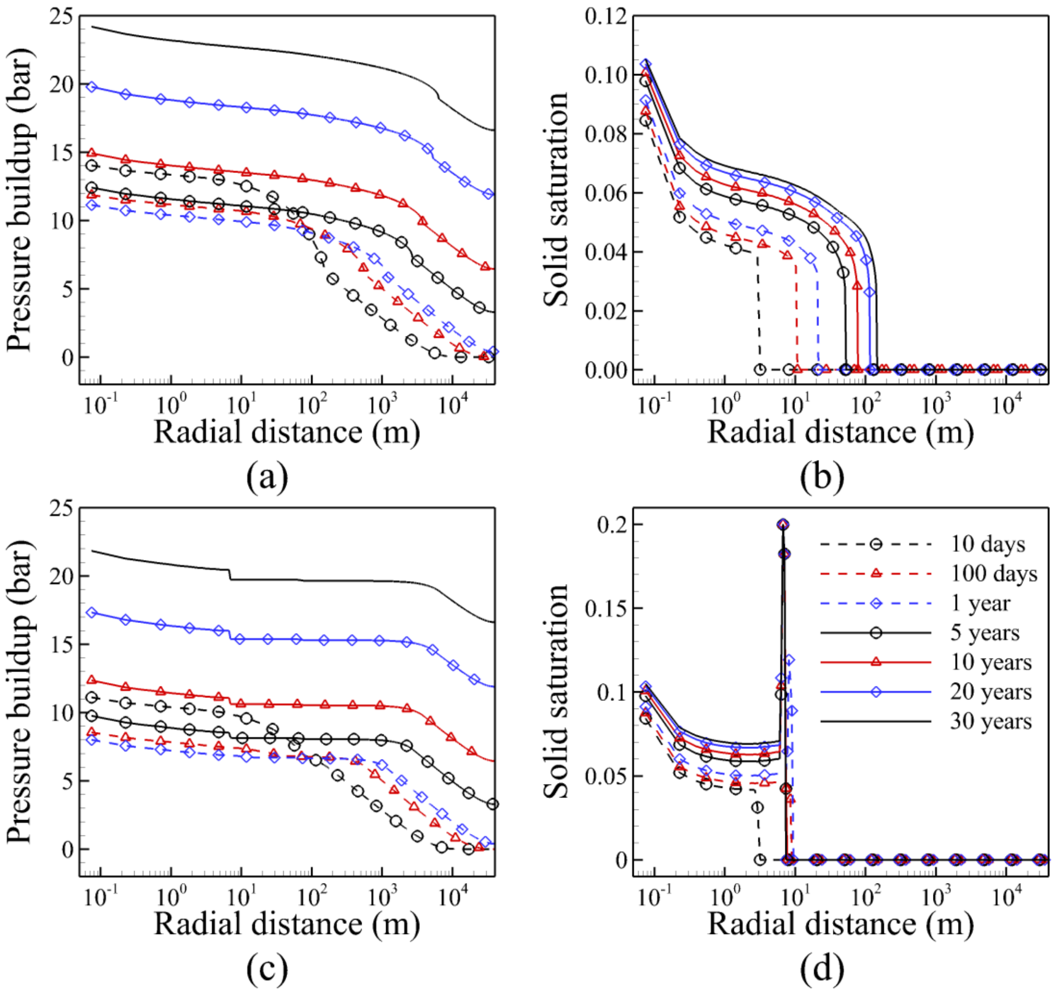

Fig. 17. Profiles of (a, c) pressure buildup (unit: bar)and (b, d) solid saturation for the semi-closed system along (a-b) the top and (c-d) the bottom of the aquifer with seal permeability of 10^{-19} m^2 at different injection time instants.

4. Conclusions

Numerical simulations have been carried out for a better understanding of the phenomena of pressure buildup and salt precipitation during CO_2 injection period for carbon storage. In order to understand the effects of boundary conditions on CO_2 storage, three storage systems with different boundary conditions have been numerically simulated and compared. This study also evaluates the flow of gas phase and the propagation of pressure, taking into account the effect of precipitation. The main conclusions from the numerical simulations are given as follows:

(1) It has been shown that the region of elevated pressure is much larger than the CO_2 plume size, while the salt precipitation due to the evaporation of gas phase only occurs in the small zone of single gas phase.

(2) The pressure change shows different behaviours for the three systems. However, the contour maps of solid saturation with the same injection rate for the three storage systems are generally similar in shape, with several small differences in precipitation zone observed for the three systems.

(3) There are two types of precipitation formed near the well, i.e., non-localized precipitation near the injection well and localized precipitation in the lower portion of the dry-out front. The evaporation of gas phase leads to precipitation near the well and the backflow of brine due to capillary pressure results in the impervious zone near the lower portion of the well. The formation processes of the two types of precipitation are different, which go through different periods. For the semi-closed system, in addition to the two types of precipitation, a third type of solid precipitation forms at the interfaces between the storage and seal formations. The salt precipitation leads to the decrease of porosity and permeability and thus the degradation of injectivity.

(4) The precipitation can affect the transportation of the gas phase and the propagation of pressure. The localized precipitation acts as a barrier that suppresses the horizontal flow of gas phase and promotes the upward flow of injected CO_2. The pressure profiles are smooth during

the early stage, while the curves reveal distinct gradients when the pores at the bottom aquifer are clogged completely. It can be concluded that the injection rate is important for the salt precipitation process. For the lower injection rate, more backflow of the brine occurs, leading to more gas phase accumulating at the aquifer top, a narrower space for the gas phase flow and a higher pressure jump at the bottom aquifer. The localized precipitation increases the risk of leakage and reduces the security of CO_2 storage.

In the present study, the salt precipitation is treated as an immobile phase that clogs the pores. In reality, the transportation of solid salt, from one location to another, can largely follow the movement of fluids such as liquids and gases. However, the flow of precipitation is very complicated and constitutive relations would be needed to specify the motion. In the future, a more sophisticated model for the movement of solid precipitation will be considered. Moreover, in order to effectively capture the dynamic behaviours of pressure buildup and salt precipitation in full-scale carbon storage, sub-grid scale dynamics may be modelled using an upscaling approach of the physical problem in a given time scale, which is being carried out.

References

[1] Bachu S. CO_2 storage in geological media: role, means, status and barriers to deployment. Prog Energy Combust Sci 2008;34:254-73.

[2] Metz B, Davidson O, de Coninck H, Loos M, Meyer L. IPCC special report on carbon dioxide capture and storage. Cambridge University Press, Cambridge, United Kingdom and New York, USA; 2005.

[3] Jiang X. A review of physical modelling and numerical simulation of long-term geological storage of CO_2. Appl Energy 2011;88:3557-66.

[4] Mathias S, González Martínez de Miguel G, Thatcher K, Zimmerman R. Pressure buildup during CO_2 injection into a closed brine aquifer. Transp Porous Med 2011;89:383-97.

[5] Yamamoto H, Zhang K, Karasaki K, Marui A, Uehara H, Nishikawa N. Numerical investigation concerning the impact of CO_2 geologic storage on regional groundwater flow. Int J Greenh Gas Con 2009;3:586-99.

[6] Zhou Q, Birkholzer JT, Tsang C-F, Rutqvist J. A method for quick assessment of CO_2 storage capacity in closed and semi-closed saline formations. Int J Greenh Gas Con 2008;2:626-39.

[7] Pruess K, Müller N. Formation dry-out from CO_2 injection into saline aquifers: 1. Effects of solids precipitation and their mitigation. Water Resour Res 2009;45:W03402.

[8] Kim KY, Han WS, Oh J, Kim T, Kim JC. Characteristics of salt-precipitation and the

associated pressure build-up during CO_2 storage in saline aquifers. Transp Porous Med 2012;92:397-418.

[9] Mathias SA, Gluyas JG, González Martínez de Miguel GJ, Hosseini SA. Role of partial miscibility on pressure buildup due to constant rate injection of CO_2 into closed and open brine aquifers Water Resour Res. 2011;47:W12525.

[10] Zeidouni M, Pooladi-Darvish M, Keith D. Analytical solution to evaluate salt precipitation during CO_2 injection in saline aquifers. Int J Greenh Gas Con 2009;3:600-11.

[11] Pruess K. Formation dry-out from CO_2 injection into saline aquifers: 2. Analytical model for salt precipitation. Water Resour Res 2009;45:W03403.

[12] Muller N, Qi R, Mackie E, Pruess K, Blunt MJ. CO_2 injection impairment due to halite precipitation. Energy Procedia 2009;1:3507-14.

[13] Mahadevan J, Sharma M, Yortsos Y. Water removal from porous media by gas injection: experiments and simulation. Transp Porous Med 2007;66:287-309.

[14] Giorgis T, Carpita M, Battistelli A. 2D modeling of salt precipitation during the injection of dry CO_2 in a depleted gas reservoir. Energy Convers Manag 2007;48(6):1816-26.

[15] Zhou Q, Birkholzer JT. On scale and magnitude of pressure build-up induced by large-scale geologic storage of CO_2. Greenh Gases: Sci Technol 2011;1:11-20.

[16] Pau GSH, Bell JB, Pruess K, Almgren AS, Lijewski MJ, Zhang KN. High-resolution simulation and characterization of density-driven flow in CO_2 storage in saline aquifers. Adv Water Resour 2010;33:443-55.

[17] Birkholzer JT, Zhou Q, Tsang C-F. Large-scale impact of CO_2 storage in deep saline aquifers: A sensitivity study on pressure response in stratified systems. Int J Greenh Gas Con 2009;3:181-94.

[18] Cihan A, Birkholzer JT, Zhou Q. Pressure buildup and brine migration during CO_2 storage in multilayered aquifers. Ground Water 2012;51:1-16.

[19] Saripalli P, McGrail P. Semi-analytical approaches to modeling deep well injection of CO_2 for geological sequestration. Energy Convers Manag 2002;43(2):185-98.

[20] Nordbotten JM, Celia MA, Bachu S. Similarity solutions for fluid injection into confined aquifers. J Fluid Mech 2006;561:307-27.

[21] Nordbotten JM, Celia MA, Bachu S. Injection and storage of CO_2 in deep saline aquifers: Analytical solution for CO_2 plume evolution during injection. Transp Porous Med 2005;58:339-60.

[22] Okwen RT, Stewart MT, Cunningham JA. Temporal variations in near-wellbore pressures during CO_2 injection in saline aquifers. Int J Greenh Gas Con 2011;5:1140-8.

[23] Nicot JP. Evaluation of large-scale CO_2 storage on fresh-water sections of aquifers: An example from the Texas Gulf Coast Basin. Int J Greenh Gas Con 2008;2:582-93.

[24] Birkholzer JT, Zhou Q, Tsang CF. Large-scale impact of CO_2 storage in deep saline aquifers: A sensitivity study on pressure response in stratified systems. Int J Greenh Gas Con 2009;3:181-94.

[25] Environment Protection Agency. Federal requirements under the underground injection control (UIC) program for carbon dioxide (CO_2) geological sequestration (GS) wells;

proposed rule; 2008.

[26] Rutqvist J, Birkholzer JT, Cappa F, Tsang CF. Estimating maximum sustainable injection pressure during geological sequestration of CO_2 using coupled fluid flow and geomechanical fault-slip analysis. Energy Convers and Manag 2007;48:1798-807.

[27] Rutqvist J, Birkholzer JT, Tsang CF. Coupled reservoir–geomechanical analysis of the potential for tensile and shear failure associated with CO_2 injection in multilayered reservoir–caprock systems. Int J Rock Mech Min Sci 2008;45:132-43.

[28] Zhang Z, Agarwal R. Numerical simulation and optimization of CO_2 sequestration in saline aquifers. Comput Fluids 2013;80:79-87.

[29] Wan LJ, Li KL, Liu J, Li KQ. GPU implementation of a parallel two-list algorithm for the subset-sum problem. Concurrency Computat: Pract Exper 2015; 27:119–145.

[30] Yang WD, Li KL, Liu Y, Shi L, Wan LJ. Optimization of quasi-diagonal matrix-vector multiplication on GPU. Int J High Perform C 2014;28(2):183-195.

[31] Jie L, Li KL, Shi L, Liu RS, Mei J. Accelerating solidification process simulation for large-sized system of liquid metal atoms using GPU with CUDA. J Comput Physics 2014; 257: 521-535.

[32] Wang YX, Zhang LL, Liu W, Che YG, Xu CF, Wang ZH, Zhuang Y. Efficient parallel implementation of large scale 3D structured grid CFD applications on the Tianhe-1A supercomputer. Comput Fluids 2013;80:244-250.

[33] Peysson Y, Bazin B, Magnier C, Kohler E, Youssef S. Permeability alteration due to salt precipitation driven by drying in the context of CO_2 injection. Energy Procedia

2011;4:4387-94.

[34] Kim M, Sell A, Sinton D. Aquifer-on-a-Chip: understanding pore-scale salt precipitation dynamics during CO_2 sequestration. Lab Chip 2013;13:2508-18.

[35] Hurter S, Berge J, Labregere D. Simulations for CO_2 injection projects with compositional simulator. In: SPE 108540, Offshore Europe, Aberdeen, Scotland, UK; 2007.

[36] Piri M, Prévost JH, Fuller R. Carbon dioxide sequestration in saline aquifers: evaporation, precipitation and compressibility effects. In: Fourth Annual Conference on Carbon Capture and Sequestration; 2–5 May, Alexandra Virginia; 2005.

[37] Prévost JH, Fuller R, Altevogt AS, Bruant R, Scherer GW. Numerical modeling of carbon dioxide injection and transport in deep saline aquifers. In: Proceedings, 7th International Conference on Greenhouse Gas Control Technologies, Vancouver, BC, vol II (2), Poster Papers Elsevier Ltd; 2004.

[38] Helmig R. Multiphase flow and transport processes in the subsurface: a contribution to the modeling of hydrosystems. Berlin: Springer; 1997.

[39] Bear J. Dynamics of fluids in porous media. New York: McGraw-Hill; 1972.

[40] Van Genuchten MT. A closed-form equation for predicting the hydraulic conductivity of unsaturated soils. Soil Sci Soc Am J 1980;44:892-8.

[41] Corey AT. The interrelation between gas and oil relative permeabilities. Prod Mon.1954;19:38-41.

[42] Spycher N, Pruess K. CO_2-H_2O mixtures in the geological sequestration of CO_2. II.

Partitioning in chloride brines at 12–100°C and up to 600 bar. Geochim Cosmochim Acta 2005;69:3309-20.

[43] Nelson PH. Permeability-porosity relationships In sedimentary rocks. The Log Analyst 1994;35:38-62.

[44] Verma A, Pruess K. Thermohydrological conditions and silica redistribution near high-level nuclear wastes emplaced in saturated geological formations. J Geophys Res: Solid Earth 1988;93:1159-73.

[45] Saad Y. Iterative methods for sparse linear systems. SIAM, Philadelphia, PA, second edition, 2003.

Figure Captions.

Fig. 1. Schematic representation of (a) CO_2 injection into a closed aquifer via a vertical well and (b) top view.

Fig. 2. Schematic representation of boundary conditions for the three storage systems: (a) open system, (b) closed system, and (c) semi-closed system.

Fig. 3. Spatial discretization considered in this study.

Fig. 4. A 16-meshes domain partitioning on 4 processors.

Fig. 5. The radial profiles of pressure buildup and solid saturation at the aquifer top for 10 days (top) and 100 days (bottom) for the grid dependence test.

Fig. 6. Cross sections of pressure buildup (top: (b) is a zoom-in of (a)) and gas saturation (bottom: (d) is the zoom-in of (c)) for the closed system at 30 years of CO_2 injection; pressure unit: bar.

Fig. 7. Cross sections of solid saturation for the closed system at 30 years of CO_2 injection with a close-up view of non-localized precipitation.

Fig. 8. Instantaneous iso-surfaces of solid saturation for the 3D closed system at different time instants.

Fig. 9. The temporal evolution of gas saturation and solid saturation in (a) the non-localized precipitation region, (b) the localized precipitation region.

Fig. 10. Profiles along the bottom of the aquifer for the closed system at different injection time

instants for (a) pressure buildup (unit: bar) and (b) solid saturation.

Fig. 11. Spatial distributions for the closed system at 60 years of CO_2 injection of (a) gas saturation and (b) solid saturation.

Fig. 12. Profiles along the bottom of the aquifer for the closed system with injection rate of 50 kg/s at different injection time instants for (a) pressure buildup (unit: bar), and (b) solid saturation.

Fig. 13. Cross sections of (a) pressure buildup (unit: bar), (b) gas saturation and (c) solid saturation for the open system at 30 years of CO_2 injection.

Fig. 14. Profiles along the bottom of the aquifer for the open system at different injection time instants for (a) pressure buildup, and (b) solid saturation.

Fig. 15. Cross sections of pressure buildup (unit: bar) with seal permeabilities of (a) 10^{-19} m^2, (b) 10^{-18} m^2, and (c) 10^{-17} m^2 for the semi-closed system.

Fig. 16. Cross sections of solid saturation with seal permeability of (a1, a2) 10^{-19} m^2, (b1, b2) 10^{-18} m^2, and (c1, c2) 10^{-17} m^2 for the semi-closed system.

Fig. 17. Profiles of (a, c) pressure buildup and (b, d) solid saturation for the semi-closed system along (a-b) the top and (c-d) the bottom of the aquifer with seal permeability of 10^{-19} m^2 at different injection time instants.

Table Titles.

Tab. 1. Hydrogeological properties of the storage formation.

Tab. 2. Example of domain partitioning and local numbering.